
Article:
Gao, W. orcid.org/0009-0007-7929-2315, Cheng, Z., Gregory, D.A. et al. (5 more authors) (2025) Advancing synthetic bone tissue engineering materials: Nano-scale investigation into transitional Interface in carbon dots/ polymer composites. Journal of Colloid and Interface Science, 700 (Part 3). 138553. ISSN: 0021-9797

https://doi.org/10.1016/j.jcis.2025.138553

Advancing Synthetic Bone Tissue Engineering Materials: Nano-scale Investigation into Transitional Interface in Carbon Dots/ Polymer Composites

Woming Gao[1], Zeming Cheng[1,2], David A. Gregory[1,2], Alexander J. Knight[3], Alexander I. Tartakovskii[3], Cornelia Rodenburg[1,2]*, Nicholas T.H. Farr[1,2]*, Frederik Claeyssens[1,2]*

* Corresponding authors

[1]School of Chemical, Materials and Biological Engineering, Faculty of Engineering, University of Sheffield, Sheffield, UK

[2]Insigneo Institute for in Silico Medicine, Pam Liversidge Building, Sir Robert Hadfield Building, University of Sheffield, UK

[3]School of Mathematical and Physical Sciences, Hicks Building, University of Sheffield, Sheffield, UK

Additional Characterization Methods Details

Mechanical test

Tensile testing of PTMPTA and all composites was conducted using a MultiTest-dV universal testing machine (Mecmesin, Slinfold, UK). Prepolymer solutions of PTMPTA and its composites were cast into cylindrical silicone molds (100 mm diameter, 1 mm thickness), and a glass plate was placed on top to ensure a smooth surface post-curing. The samples were fully cured under 365 nm UV light using a Dymax BlueWave® FX-1250 high-intensity LED flood lamp (Dymax®, Wiesbaden, Germany) for 90 seconds. Dog-bone-shaped specimens (working area: 10 mm × 2 mm × 1 mm) were then precision-cut from the cured discs using a laser cutter (Laserscript LS3040, Trotec Laser GmbH., Boldon, UK). All tensile tests were performed using a 250 N load cell at a constant crosshead speed of 1 mm/min. Ten specimens (n = 10) were tested for each sample group.

The compressive properties of PTMPTA and all composites were evaluated using Zwick Roell AllroundLine Z050 system (ZwickRoell Ltd., Worcester, UK) with a 50 kN load cell. All tests were performed at a constant crosshead speed of 1 mm/min. The prepolymer solutions were cast into cylindrical silicone molds (9.5 mm diameter × 4 mm height), with a glass plate placed on top to ensure a flat curing surface. The samples were fully cured under 365 nm UV light using a Dymax BlueWave® FX-1250 high-intensity LED flood lamp for 90 seconds. For each material group, five replicate specimens (n = 5) were tested.

No surface polishing was applied, but the molds and laser cutting produced smooth and uniform surfaces across all specimens. The working area of all samples was averaged from three measurements.

Cross-linking density test

For cross-linking density test, equal-sized rectangular samples of the composites were prepared and immersed in toluene for one day, after which excess solvent was removed by gravity. The samples were then placed into NMR tube and were completely submerged by $CDCl_3$. 400 MHz ^1H nuclear magnetic resonance (NMR) (Burker AVIIIHD 400 NMR spectrometer (Blue Scientific Limited, Cambridge, UK)) was carried out. MestReNova software (MestreLab Research, Santiago de Compostela, Spain) was used to analyze the spectra. The cross-link density was assessed by comparing the chemical shifts of functional groups across different samples.

Swelling test

The composite samples were initially weighed (W_{dry}) and then fully immersed in deionized water, PBS (pH = 7.4), and ethanol and incubated at room temperature (25 °C). The samples were reweighed (W_{wet}) on day 1, 3, 5, 7, and 9 after removing surface liquid with filter paper. The swelling ratio was calculated using Eq. (1).

$$\text{Swelling Ratio (\%)} = [(W_{wet} - W_{dry})]/ W_{dry} \times 100 \quad (1)$$

The nano-FTIR, AFM, and s-SNOM test

The nano-FTIR, AFM, and s-SNOM data presented in Figure 5 of the main manuscript were taken using a neaSCOPE s-SNOM setup from attocube systems AG. During the nano-FTIR and s-SNOM measurements, laser light was focused down onto the tip of an AFM cantilever coated in metal (ARROW-EFM cantilevers from NanoWorld, Pt/Ir coating) in order to generate surface excitations in the tip's surface. These surface excitations are comprised of a strong, confined electric field component, which is brought into proximity with the sample during tapping mode AFM operation. This electric field probe interacts with the sample and generates a scattering centre, which then scatters further incoming light into the detection path of the system. By using an interferometer setup, with a clean reference mirror in one arm and the AFM system in the other arm, both the amplitude and phase of the scattered light can be recorded. Demodulating the measured signal at harmonics of the AFM tapping frequency, as well as moving the reference mirror (for nano-FTIR – a clean single movement of the mirror along the direction of the interferometer arm, for s-SNOM – a jittering sinusoidal motion applied to the mirror which adds a known addition to the lock-in frequency), allows for the complete suppression of background signal in the measurement data.

AFM parameters: 79kHz tapping frequency, 60-70nm tapping amplitude. The data is levelled to a plane fit.

Nano-FTIR parameters: The broadband illumination source used was a FemtoFiber dichro midIR from TOPTICA Photonic, with spectrum setting 'C' (output range approximately 900-1900 cm^{-1}). The data demodulated at the second harmonic of tapping frequency is presented. The data was referenced to a clean measurement of a silicon test sample. A moving average of five points was applied to smooth the data.

s-SNOM parameters: The illumination source used was a MIRcat-QT from Daylight Solutions operating at 1115cm^{-1}, and the data demodulated at the third harmonic of tapping frequency is presented. s-SNOM amplitude data is normalised to the maximum recorded value, and s-SNOM phase data is offset by the mean recorded value.

In-vitro degradation test

The procedures adopted for the study were conducted in accordance with the recommendations of ISO 10993-13, Biological Evaluation of Medical Devices Part 13: Identification and Quantification of Degradation Products from Polymeric Medical Devices [1]. Uniformly sized composite discs (160 mg, 15 mm diameter) were prepared and thoroughly rinsed with deionized water to remove residual prepolymer and photoinitiator from the surface. The samples were first characterized by FTIR, then immersed in PBS (simulating physiological conditions) and 3% H_2O_2 solution (simulating oxidative degradation), with a solid-to-liquid ratio of 1 g : 10 ml. Degradation was conducted at 37 °C for 14 days. Following the degradation treatment, the samples were washed with deionized water, transferred to clean collection containers, and placed on a Stuart orbital shaker S1500 (Keison Products, Essex, UK) at 115 RPM for 7 additional days. After the full 21-day treatment period, the samples were removed, air-dried at room temperature, weighed, and analysed again by FTIR. The triplicate of each sample was measured every time.

Cell culture and seeding on samples

MG63 osteoblasts (P9-P17) were revived from -80°C freezer. The culture media was based on Dulbecco's modified Eagle's medium (DMEM) and was supplemented with 10% v/v FBS, 1% v/v L-glutamine, P/S and NEAA and 4% v/v amphotericin B. The cells were incubated at 37°C, 5% CO_2 and were passaged when their confluency under light microscope reached 70% - 80%. The samples were pre-washed in PBS for 7 days for photo initiator and prepolymer removal and were laser cut into discs (15 mm diameter, 1 mm thickness). The sample discs were sticked at the bottom of 24-well plates with non-cytotoxic glue (KingBritish) and disinfected in 70% ethanol aqua solution and then washed in PBS. The cells' concentration was calculated with haemocytometer before seeding and 1×10^4 cells were seeded on each sample.

Cell viability test

The cell viability on the samples was measured via resazurin reduction assay and seeding on TCP as positive control. The resazurin sodium salt was dissolved in PBS in the concentration of 25 mg/100 ml as the master stock and was diluted 10 times in culture media as reaction solution. The MG63 cells were seeded on the scaffolds and the viability was measured on day 1, day 4 and day 7 by replacing the culture media with reaction solution and incubating in the dark at 37°C for 4 hours. Then 200 µl of the solution in each well was transferred to a 96-well plate and was read at the excitation and emission wavelengths of 540 nm and 630 nm in microplate reader (FLX800, BIO-TEK Instruments, Inc., Agilent, Santa Clara, CA, USA). After day 7, all cell-cultured media was collected for FTIR analysis. The spectra were recorded using a PerkinElmer Frontier Fourier Transform Infrared (FTIR) spectrometer (PerkinElmer, Waltham, MA, USA), with blank culture medium on TCP serving as the background reference.

Live/dead assay

1×10^4 MG63 cells were cultivated on the sample discs for 7 days and the culture media was replaced every other day. The live/dead staining solution was made by dissolving the Calcein Green AM in DMSO and dilute the Calcein Green AM DMSO solution and ethidium bromide in PBS. The staining solution was dropped on the sample surface after removing the culture media and the cells were incubated for 10 minutes at 37°C. Then the live/dead cells were imaged at 10× magnification under Nikon A1 Confocal microscope (Tokyo, Japan).

Time-dependent curing depth experiment

TMPTA and all composite prepolymer solutions were transferred into glass tubes (2 cm in diameter, 10 cm in height). To ensure unidirectional exposure, the tube caps and side walls were wrapped in aluminium foil, leaving only the bottom exposed. UV curing was initiated from the base using a M405L2 UV-mounted LED lamp (Thorlabs Inc., Newton, NJ, USA) with an intensity of 700 mW/cm² at 405 nm. Samples were irradiated for varying durations (1, 2, 5, 10, 20, and 30 seconds).

Following each exposure, unreacted monomers were removed, and the cured lengths were measured. For each time point, triplicate measurements were performed and averaged to determine the mean curing depth.

Photo-DSC Measurements

The analysis was conducted using a Pyris Diamond DSC (PerkinElmer, Shelton, CT, USA). A M405L2 UV-mounted LED lamp (Thorlabs Inc., Newton, NJ, USA; 405 nm, 700 mW/cm²) was mounted 1 cm above the open sample chamber. Approximately 5 mg of prepolymer sample—TMPTA and all composite prepolymer solutions—was placed in an aluminium DSC pan. The reference was an empty pan. All measurements were performed at 30°C under a nitrogen atmosphere. The UV light source was controlled via a Thorlabs development controller and triggered after a 1-second temperature equilibration. Samples were irradiated for 10 seconds, and the resulting heat flow was continuously recorded.

Dynamic light scattering (DLS)

A Zetasizer Nano ZS90 Size Analyzer (Malvern Panalytical Ltd, Malvern, UK) was used to analyse the particle size of CA CDs and its aggregation. all composite prepolymer solutions were prepared and measured the particle size from 0.3nm to 10 microns (diameter) using 90 degree scattering optics.

Statistical analysis

Differences between groups were assessed using EXCEL standard deviation analysis (STDEV), Originlab 2023's and GraphPad Prism one-way Analysis of Variance (ANOVA) test (for mechanical test, resazurin and water contact angle test), and the results were plotted as mean ± standard deviation (SD). Significant differences between each experimental group were analyzed. Significant difference was defined as *$p < 0.05$. Highly significant differences were defined as **$p < 0.01$, ***$p < 0.001$, and ****$p < 0.0001$.

SEM image for 8% CA CDs/PTMPTA composites

Cryo-scanning electron microscopy (Cryo-SEM) was conducted using the Quorum PP3010T cryo-SEM preparation system (Quorum Technologies Ltd., Laughton, East Sussex, UK). Specimens were mounted on a cryo-SEM shuttle, and plunge-frozen in slushed liquid nitrogen. The shuttle was then transferred to a cooled prep stage (-160 °C) before being loaded onto the cryo-stage (-160 °C) housed within the SEM chamber for imaging. An anti-contaminator was also placed within the chamber at a temperature of -185 °C.

A FEI Helios Nanolab G3 (FEI Company, US) microscope was employed for surface morphology observations of 8% CA CDs/PTMPTA composites. In contrast to common scanning electron microscopy (SEM) analysis practice, samples were not pre-treated with a conductive coating by deposition. An accelerating voltage of 1-2 keV at typical chamber vacuum pressures in the range of 10−6 mbar and a working distance of 4 mm were chosen to avoid sample damage through surface charging. An Everhart-Thornley Detector (ETD) was selected for SEM image.

Additional Experimental and Characterization Details

1. Characterization of CA CDs

Upon microwave irradiation the citric acid solution turns yellow and finally orange during its carbonisation process, which indicates the formation of CA CDs (Figure S1A) [2]. Upon completion of the reaction, the products are dispersed in water and centrifuged, neutralized and dialyzed to remove insoluble particles in water and small molecules. The resulting solution is then dried to obtain CA CDs powder (Figure S1B).

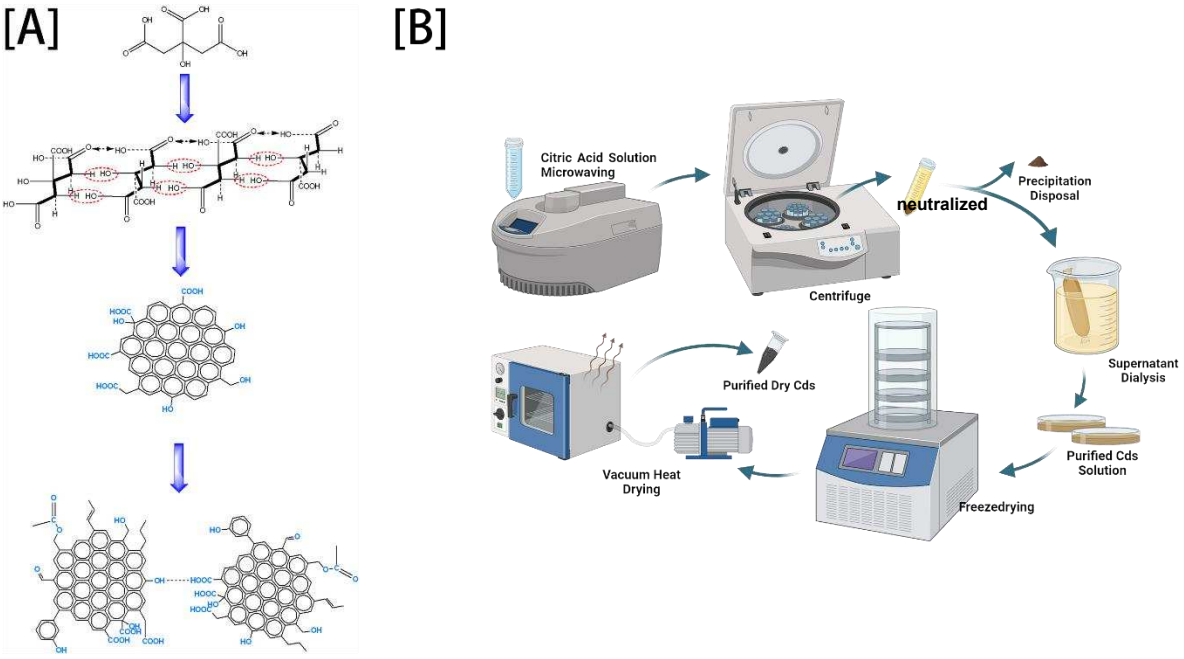

Figure S1. (A) the synthesis of CA CDs; (B) The production process of CA CDs.

We explore the chemical structures of the CA CDs, XRD, FTIR, NMR and XPS characterization of CDs was conducted. In XRD pattern (Figure S2A), the appearance of a broad peak at approximately 20° further indicates the high degree of graphitization within the CD core. This broad peak corresponds to a graphite-like structure, with an interlayer distance of 0.44 nm (002). Compared to the 0.335 nm layer spacing of pure graphite, the increased spacing may be attributed to the steric hindrance of functional groups at the edges of the sp^2-carbon planes or to planar distortion caused by sp^3 carbon within the sp^2-carbon domain [3]. Additionally, a minor peak was observed at $2\theta = 43°$ in the XRD pattern, which corresponds to the (100) plane of graphene with a lattice fringe spacing of 0.21 nm [4].

According to FTIR result (Figure S2B), the peak around 3500 cm^{-1} is attributed to the O-H

stretching on hydroxyls and phenols. The peaks in the 3000-3100 cm^{-1} range correspond to the =C-H stretching vibration of aromatic and alkenes, while those around 2850 cm^{-1} are associated with the -C-H stretching vibration of saturated hydrocarbons. The peak at approximately 1688 cm^{-1} can be assigned to C=O on ketones, aldehydes, carboxylic acids, esters or C=C on alkenes. The fingerprint region peaks around 1350-1470 cm^{-1} are indicative of the bending or deformation vibrations of C-H on methyl and methylene groups, and the region between 1000-1350 cm^{-1} corresponds to the C-O stretching vibration on alcohol, phenol, ether and carboxylic acid. Peaks below 1000 cm^{-1} are attributed to -C-H bending vibration in aromatic hydrocarbon substituents. The above results revealed the presence of various functional groups on the CA CDs including hydrocarbons, hydroxyls, carbonyls, esters, and aromatic rings.

For NMR, both ^{1}H and ^{13}C NMR spectroscopy were done to further confirm CA CDs' structures. According to ^{1}H NMR (Figure S2C), the signal around 0.8 ppm (a) corresponds to the methyl hydrogen; The signals around 2.0 ppm (b) can be attributed to CH_2 groups adjacent to a carboxylic group; The signal around 2.8 ppm and 3.0 ppm (c, d) both split into 2 peaks, which can be attributed to protons on CH groups adjacent to hydroxyl, protons on hydroxyl groups and residual citric acid. Signals near 3.37 ppm (e) are assigned to CH_2 protons connected to ester or ether groups; The signals between 5.5 to 7 ppm (g, h) correspond to aromatic or unsaturated CH [5]. Figure S2D presents the ^{13}C NMR spectrum. The signals between 20 and 30 ppm (1) correspond to CH_3 groups; Signals around 40 ppm (2) are attributed to CH_2 carbons adjacent to sp^2-hybridized carbons or oxygen atoms, while those between 60-80 ppm (3) represents quaternary carbon, C-O or C-O carbons. Two signals between 130-140 ppm (4, 5) correspond to sp^2-hybridized carbons (C=C) and C=O on aromatic rings. The peaks between 160-180 ppm (6) are indicative of the C=O on the carboxyl group [6]. The additional peaks observed at 43, 73, 173, and 176 ppm (labelled as CA) are consistent with residual citric acid, as confirmed by the simulation of the ^{13}C NMR spectrum of citric acid (Figure S6). The integration of the peaks in the ^{13}C NMR spectra was subsequently calculated to determine the percentage distribution of carbon atoms in different chemical environments (Figure S7). As presented in Table S1, the content of sp^3 carbon and carbon in C-O groups was determined to be 37.19%, while sp^2 carbon and C=O groups associated with aromatic rings accounted for 40.22%. Additionally, the carboxyl group carbon constituted 22.59% of the total carbon content.

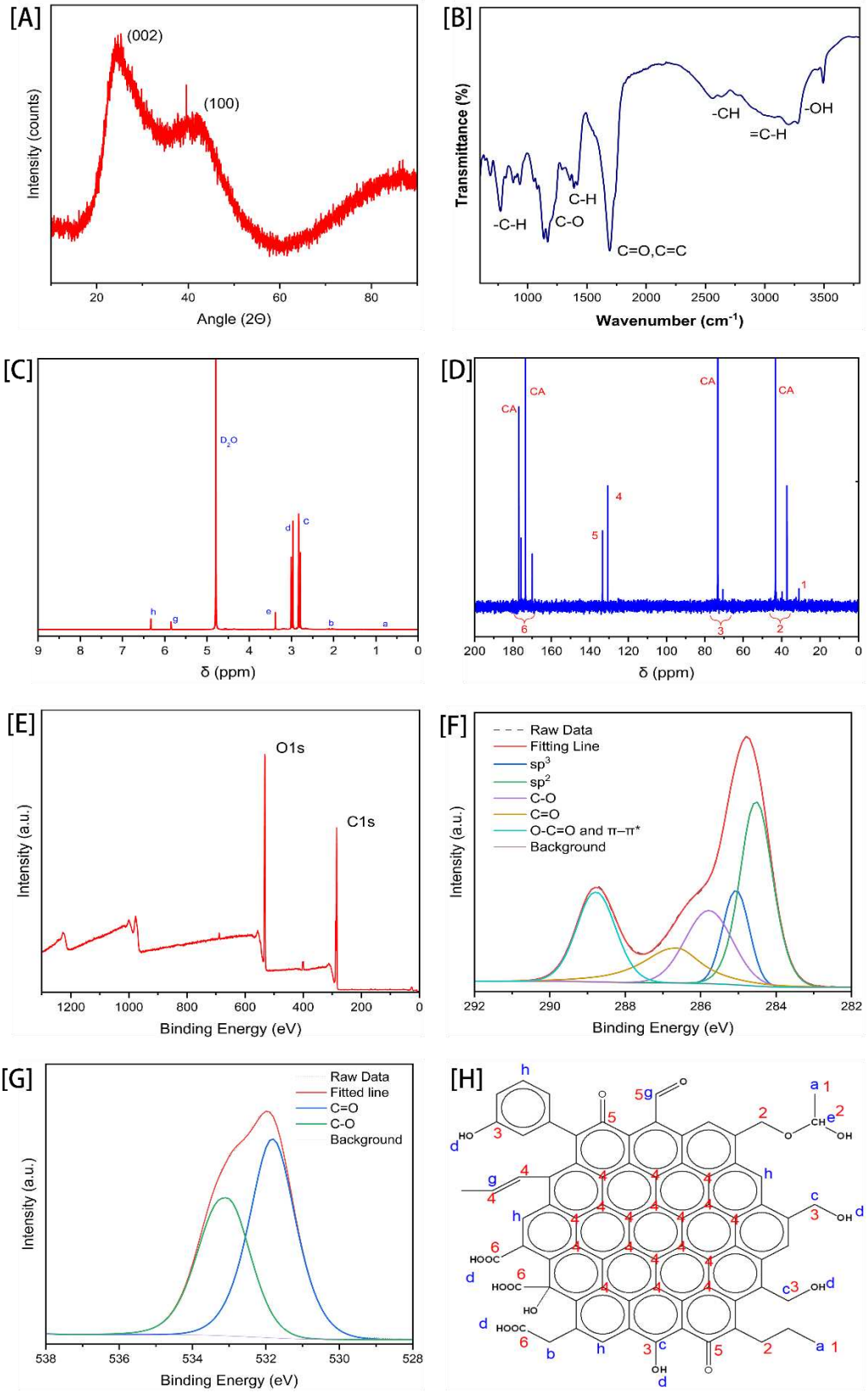

Figure S2. Structural characterizations of CA CDs: (A) XRD spectrum; (B) FTIR spectrum; (C) ^{1}H-NMR spectrum and (D) ^{13}C-NMR spectrum recorded in D_2O; (E) full XPS survey and high-resolution (F) C 1s and (G) O 1s XPS spectra; (H) molecular structure model of CA CDs according to previous spectra.

Table S1 Comparison of carbon group content measured by ^{13}C NMR and C1s XPS spectrum (Left: 13C NMR; Right: C1s XPS)

^{13}C NMR				C1s XPS			
Signal	Percentage of Signal Area (%)	Carbon group	Content of the group (%)	Peaks	Percentage of Signal Area (%)	Carbon group	Content of group (%)
1	1.99	sp^3 C and C-O	37.19	sp^3	13.71	sp^3 C and C-O	32.77
2	31.23						
3	3.97			C-O	19.06		
4	25.27	C=O on aromatic ring and sp^2 C	40.22	sp^2	34.22	sp2 and C=O	47.53
5	14.95			C=O	13.31		
6	22.59	carboxyl group C	22.59	carboxyl group	19.69	O-C=O	19.69

Figure S2E-G are the XPS patterns, the full survey spectrum (Figure S1E) reveals peaks corresponding to C1s (284.8 eV) and O1s (532.3 eV), indicating that CA CDs primarily consist of carbon and oxygen elements. Trace nitrogen peaks are also detected, which may result from impurities or reactions involving nitrogen in the air during the pyrolysis process; these can be considered negligible. The high-resolution XPS spectrum of C 1s (Figure S1F), after deconvolution, reveals four components: sp^3 C around 284.5 eV, sp^2 (graphitic) C around 285 eV, C-O around 285. 8 eV, and C=O around 287 eV, as well as a carboxyl group and π-π* combined peak around 288.8 eV. Similarly, the O 1s spectrum deconvolution (Figure S1G) identifies two contributions: C-O at 531.8 eV and C=O at 533 eV [6],[7]. Subsequently, the relative composition of each component was quantified based on the area under the C 1s and O1s curve. Analysis of the C 1s spectra (Table S1) revealed that the content of sp^2 carbon was 34.22%, sp^3 carbon was 13.71%, C-O was 19.0%, C=O was 13.31%, and the carboxyl group along with the π-π* contribution accounted for 19.69%. Similarly, the O 1s spectra indicated that the contributions of C-O and C=O oxygen were nearly equivalent, comprising 49.34% and 50.66%, respectively. Table 1 presents a comparison of the carbon group content as measured by ^{13}C NMR and XPS. While some discrepancies in the values are observed, these differences may be attributed to instrumental and calculation errors, as well as the presence of residual citric acid. Nevertheless, the variations are relatively minor.

Based on the above XRD, FTIR, NMR and XPS structural characterization and previous related literature [3], [9], [10], [11], we proposed a molecular structure model of CA CDs (Figure S2H), and CA CDs molecules might underwent π-π stacking interactions, forming integrated structures resembling graphite or pyrolytic carbon [4]. Single CA CDs molecule consisted of at least 19 fused aromatic rings, resulting in a molecular weight that can exceed 1 kDa. This is consistent with the 1 kDa molecular weight cutoff of the dialysis bag used for purification. The core of the CA CD consisted of a polycyclic aromatic hydrocarbon (PAH) structure, with its surface functionalized by various groups.

2. Synthesis of CA CDs /PTMPTA composites

To obtain CA CDs /PTMPTA composites, the purified CA CDs were mixed with the TMPTA prepolymer solution, at the mass ratio of 0%, 2%, 4%, 6%, 8% and 10% to PTMPTA. The mixtures were initially thoroughly dispersed in ethyl acetate (Figure S3A), and then placed in the vacuum until ethyl acetate was fully evaporated, the resulting uniformly mixed CA CDs/PTMPTA prepolymer was subsequently cured under 365nm UV lamp for 90s, forming the final composites (2% CA CDs/PTMPTA composites, 4% CA CDs/PTMPTA composites, 6% CA CDs/PTMPTA composites, 8% CA CDs/PTMPTA composites, and 10% CA CDs/PTMPTA composites). Upon observation, the colour of the prepolymer solution and the cured composites progressively turned more yellow as the concentration of CA CDs increased, suggesting that the CA CDs were successfully integrated into the PTMPTA matrix (Figure S3B and S3C from left to right). When the CA CDs content exceeded 8%, precipitation occurred in the solution, rendering it turbid, and the sample disk becomes opaque, with visible solid aggregates of CA CDs embedded within the composites. This indicates that 8% CA CDs is the maximum concentration that can be uniformly dispersed within the composites.

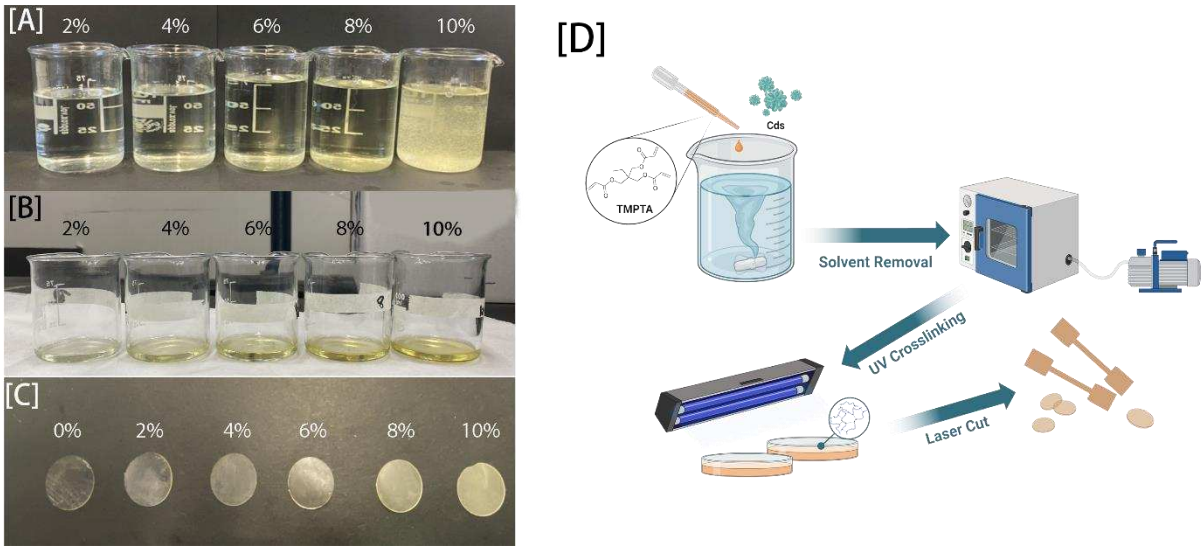

Figure S3. (A) different ratio of CA CDs and TMPTA prepolymer dispersed in ethyl acetate (from left to right: 2% CA CDs, 4% CA CDs, 6% CA CDs, 8% CA CDs, 10% CA CDs and TMPTA in ethyl acetate). (B) the ethyl acetate was removed, and left CA CDs well dispersed in TMPTA prepolymer (from left to right: 2% CA CDs, 4% CA CDs, 6% CA CDs, 8% CA CDs, 10% CA CDs and TMPTA). (C) PTMPTA and CA CDs/PTMPTA composites were made after photocuring (from left to right: PTMPTA, 2% CA CDs /PTMPTA composites, 4% CA CDs /PTMPTA composites, 6% CA CDs /PTMPTA composites, 8% CA CDs /PTMPTA composites, 10% CA CDs /PTMPTA composites). (D) The process flow of making CA CDs/PTMPTA composites.

3. Characterization of swell ratio of CA CDs /PTMPTA composites

The swelling behaviour of the scaffolds is also a crucial indicator for in vivo grafts. The swelling rate significantly impacts the overall performance and efficacy of the scaffolds [12]. Figure S4A-C illustrates the swelling rate of materials over time when immersed in ethanol, deionized water (DI) and PBS respectively. The data indicate that the swelling rate increases with time, reaching a maximum and stabilizing on the 7th day. Generally, the swelling rate of materials is inversely related to their crosslinking density; that is, a higher the swelling rate indicates a lower crosslinking

density [13]. Consequently, we compared the swelling rate with the cross-linking density, revealed that 2% CA CDs/PTMPTA composites, which exhibit the highest cross-linking density, also demonstrate the lowest swelling rate. Conversely, the 10% CA CDs/PTMPTA composites, characterized by the lowest cross-linking density, show the highest swelling rate. However, although the cross-linking density of 4% and 6% CA CDs/PTMPTA composites is higher than that of PTMPTA, the observed swelling rates are contrary to expectations. This anomaly may be attributed to the aggregation of CA CDs within the polymer matrix and their contribution to the overall hydrophilicity of the composites, which facilitates liquid ingress and consequently enhances swelling [14]. Water contact angle measurements (Figure 6K) confirmed an increase in hydrophilicity with increasing CA CDs content. In addition, SEM images of the composites (Figure S13) revealed pronounced aggregation of CA CDs on the surface, with higher CD content leading to more extensive and larger clustering. Compared to all the materials tested in various liquid (Figure S4D), the highest swelling rate observed is approximately 21.5% for the 10% CA CDs/PTMPTA composites in ethanol. In PBS, the maximum swelling rate for the 10% CA CDs/PTMPTA composites is around 14%, with other materials exhibiting swelling rates of 10% or lower. These results indicate that all composites possess relatively low swelling properties [15].

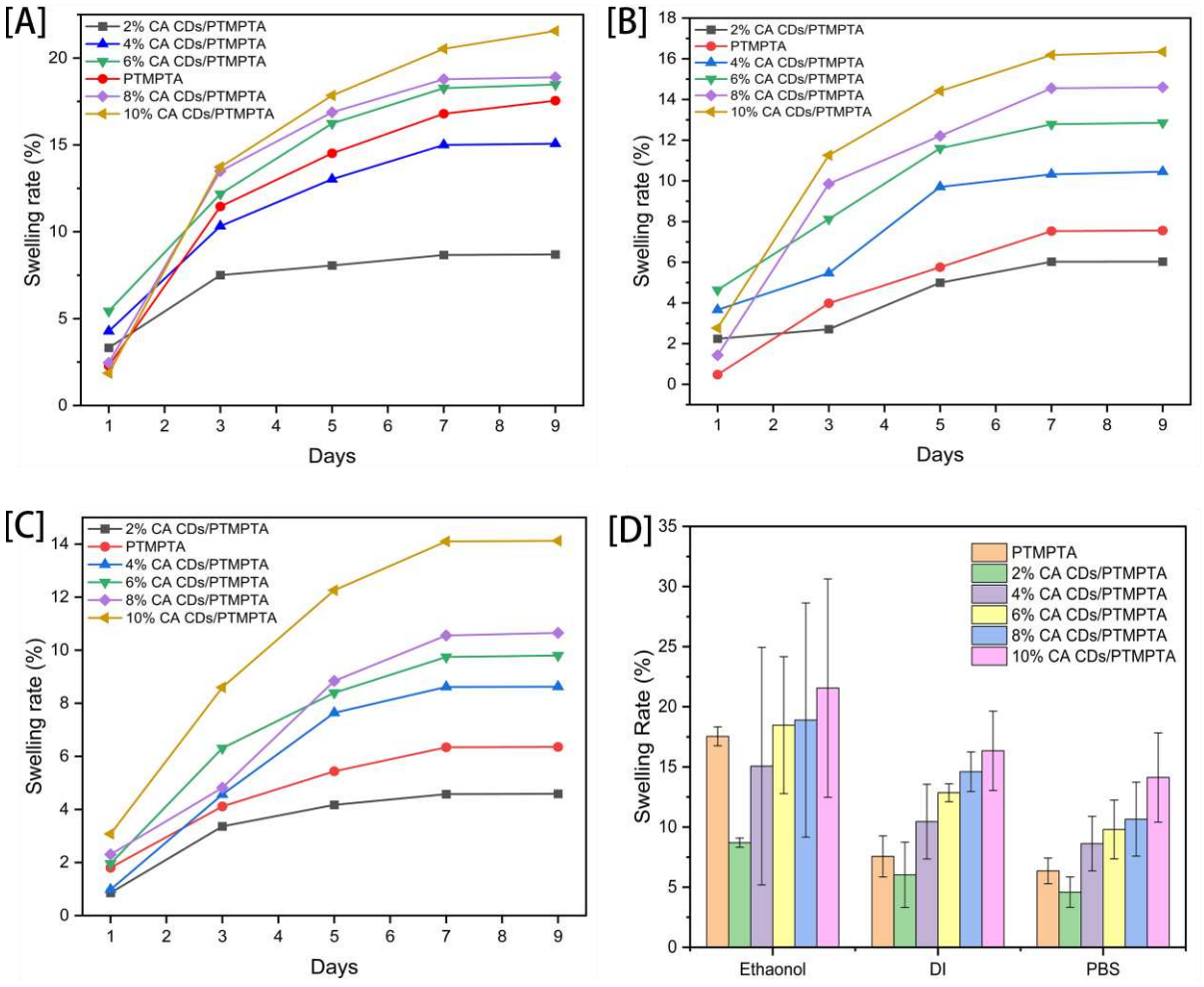

Figure S4. Changes in swelling rates of PTMPTA and CA CDs/PTMPTA composites in (A) ethanol, (B) deionized water and (C) PBS were measured within 9 days. (D): Compared the swelling rate (%) of PTMPTA and CA CDs/PTMPTA composites in ethanol, deionized water, PBS at 9 days.

Supplementary Figures and Tables

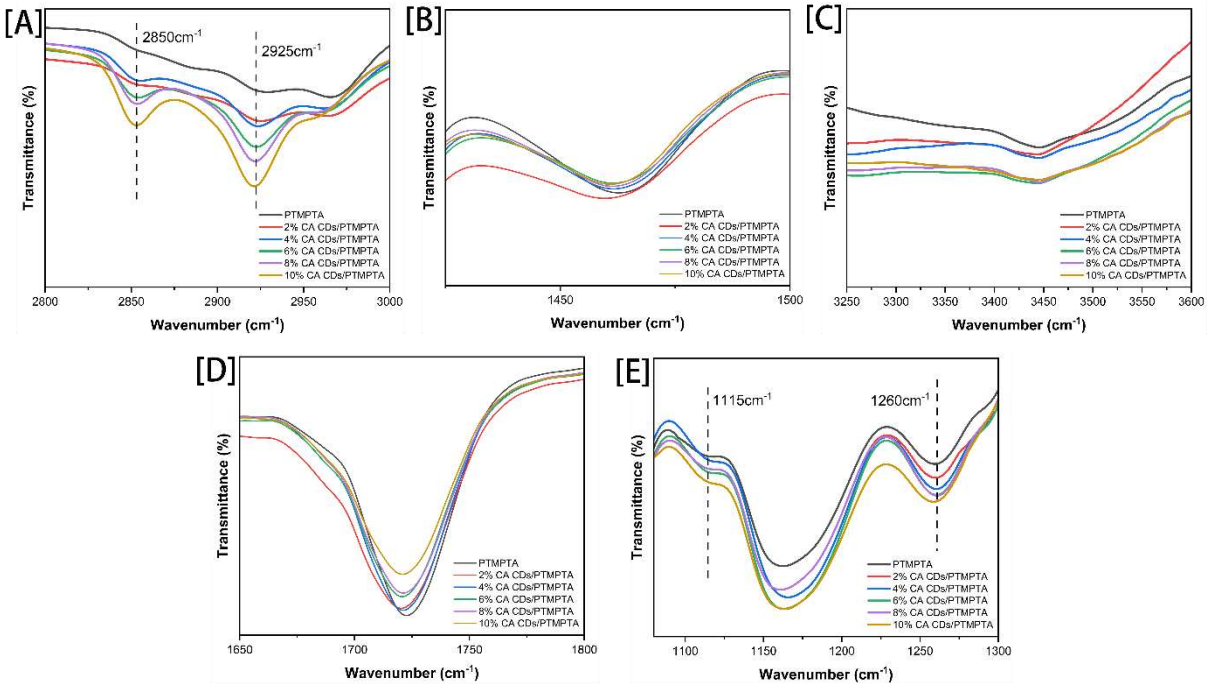

Figure S5. Partially enlarged views of the FTIR spectra of PTMPTA and CA CDs/PTMPTA composites: (A) The peaks at 2925 cm^{-1} and 2850 cm^{-1}. (B) The peak at 1460 cm^{-1}. (C) The peak at 3440 cm^{-1}. (D) The peak at 1722 cm^{-1}. (E) The peaks at 1260 cm^{-1} and 1115 cm^{-1}

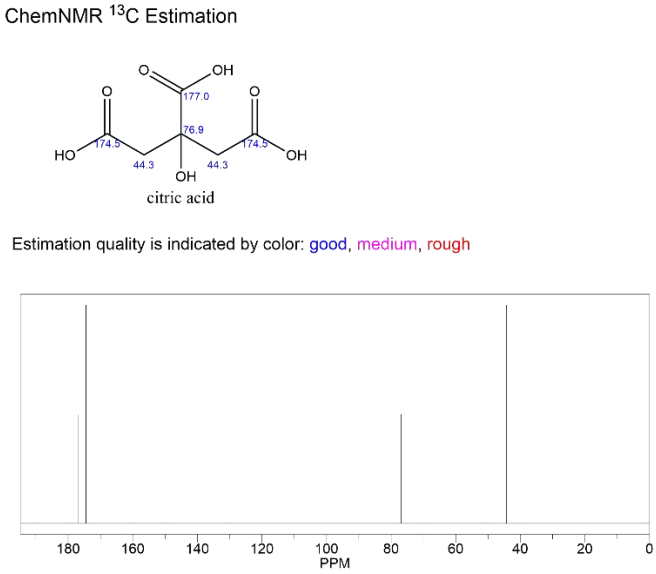

Figure S6. Predicted C NMR spectra of citric acid

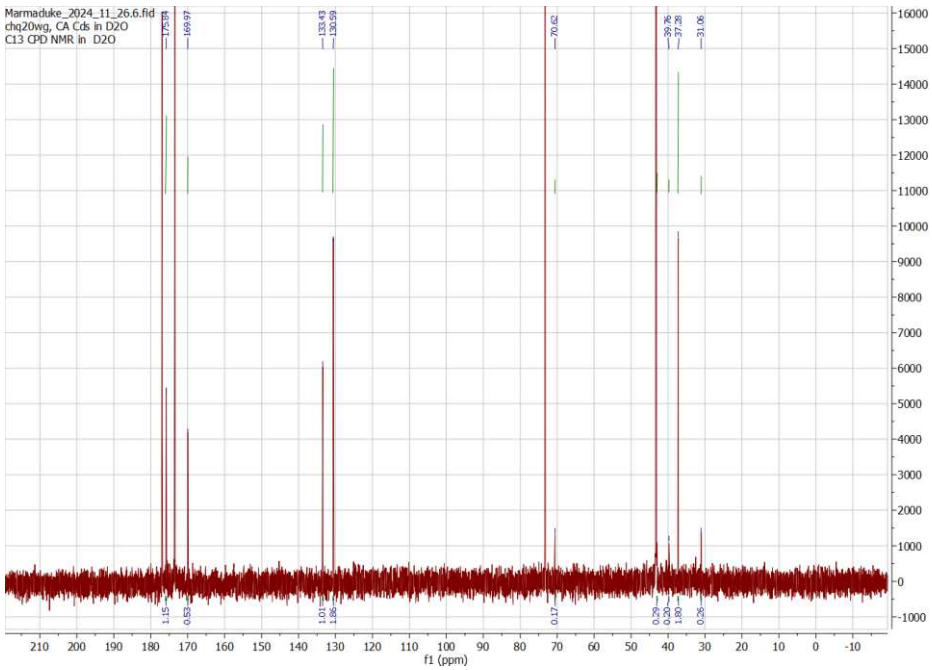

Figure S7. Integration analysis of 13C NMR of CA CDs

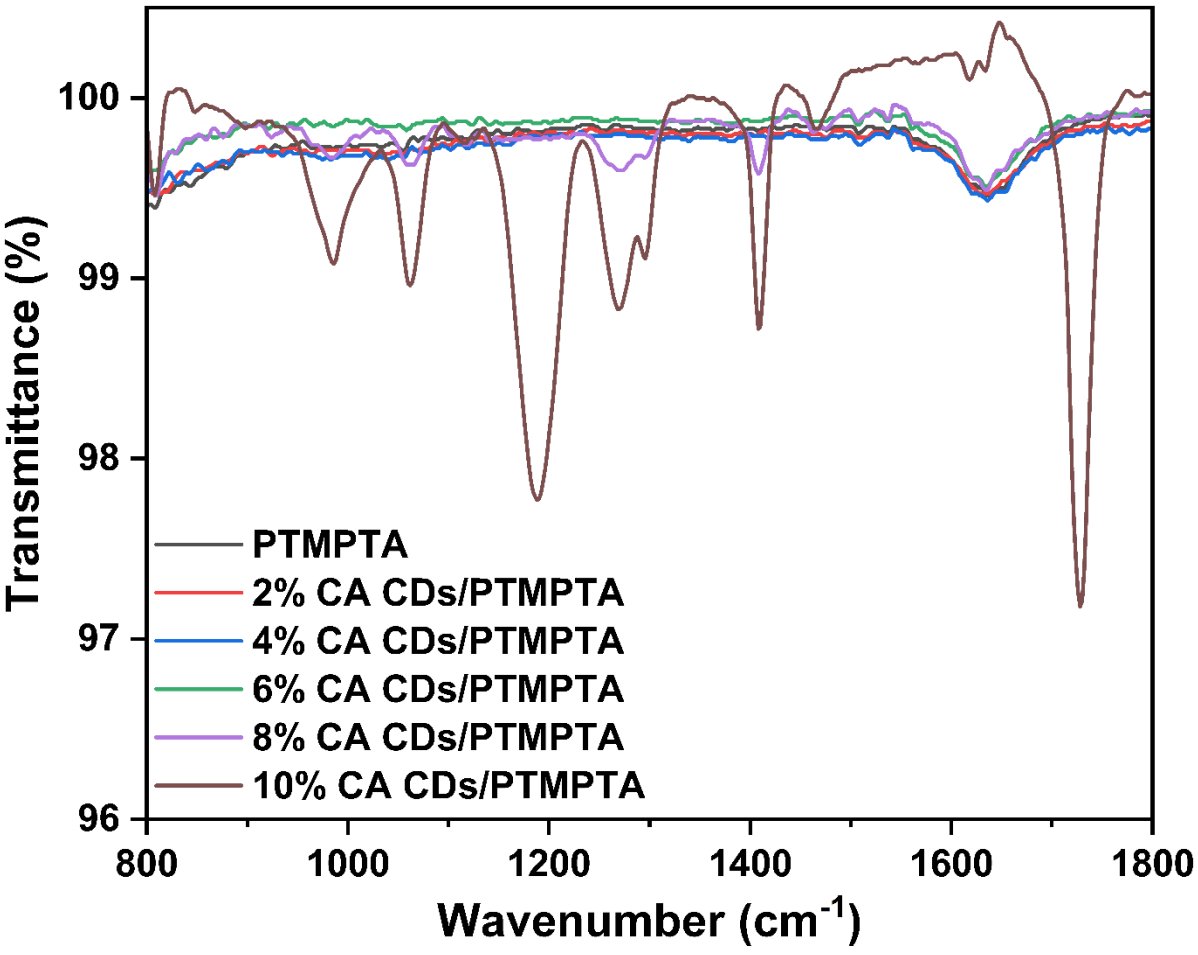

Figure S8. FTIR spectra of cell-cultured media after 7days cell viability test.

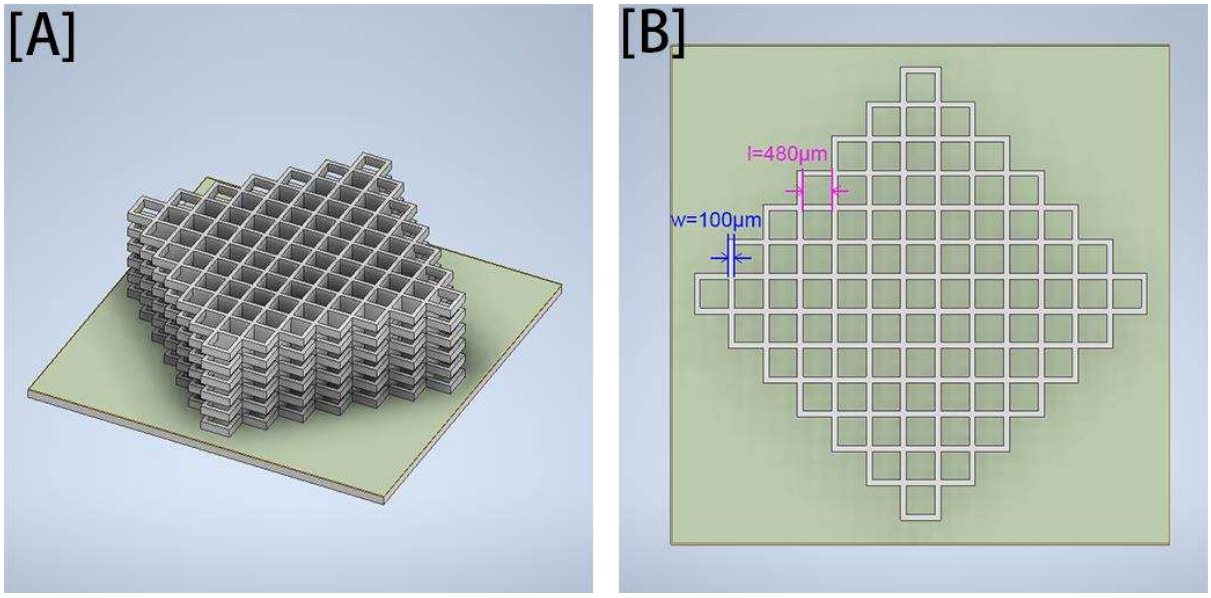

Figure S9. (A) The self-designed woodpile structure and (B) its top view, marking the square holes with a side length of 480 μm and microstructure widths of 100 μm (l × w = 480 μm × 100 μm)

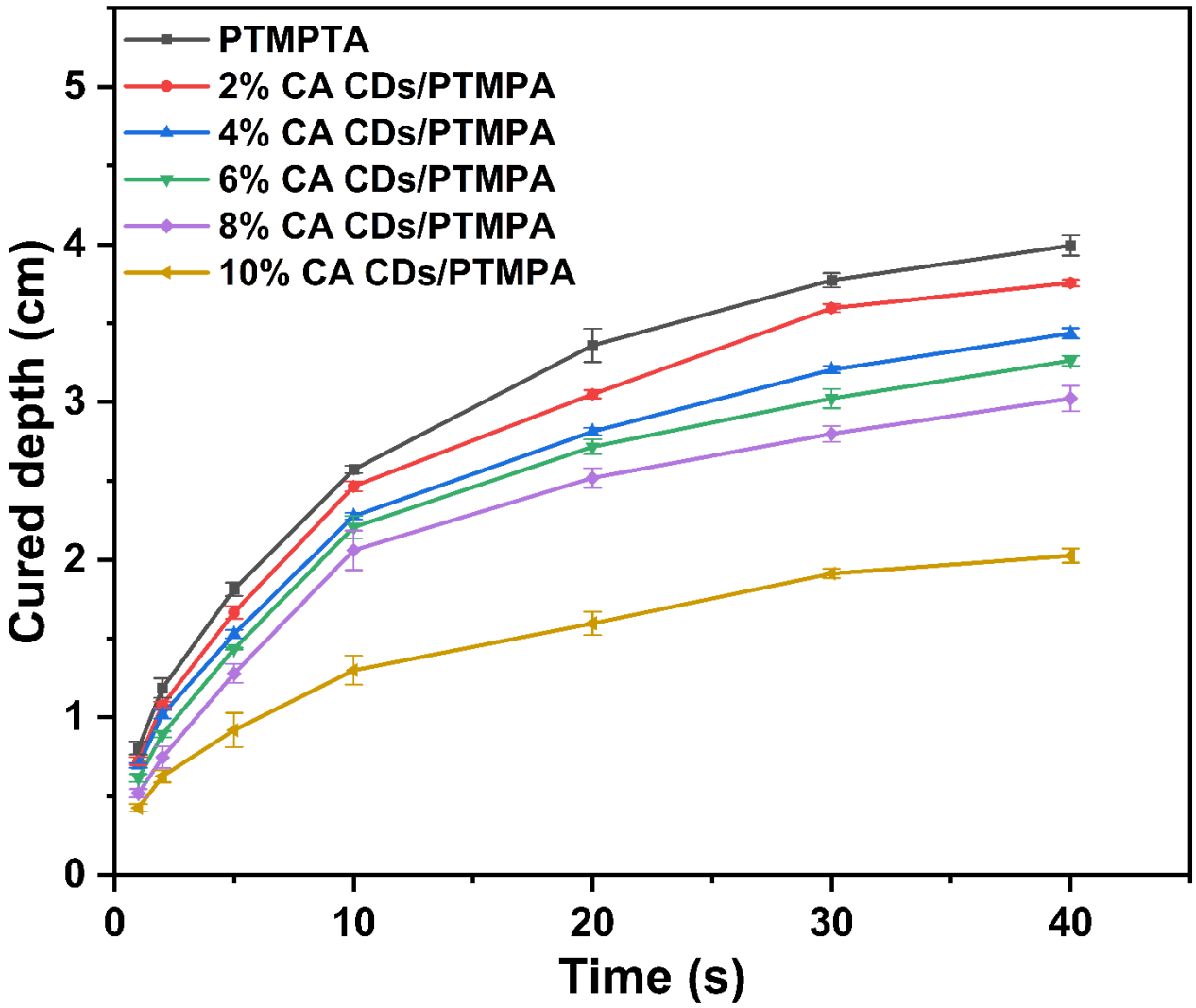

Figure S10. Photocuring depth of PTMPTA and all composites' samples upon 405 nm UV irradiation for different time. Light intensity was 700 mW/cm^2.

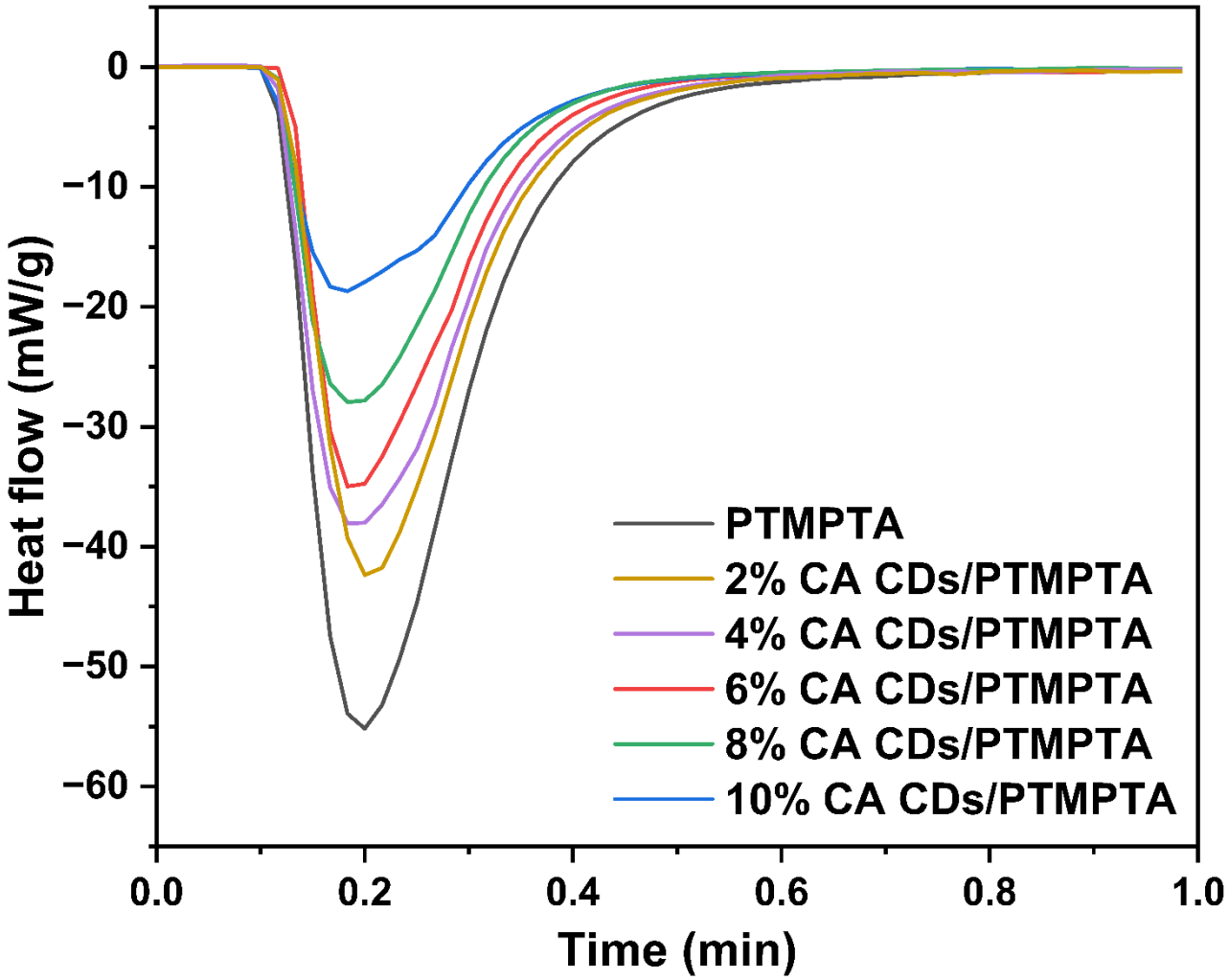

Figure S11. Photo DSC of PTMPTA and all composites prepolymer solutions under 405 nm UV light. Amount on sample in the pan was 5 mg. Measurements were taken under nitrogen. Light intensity was 700 mW/cm^2.

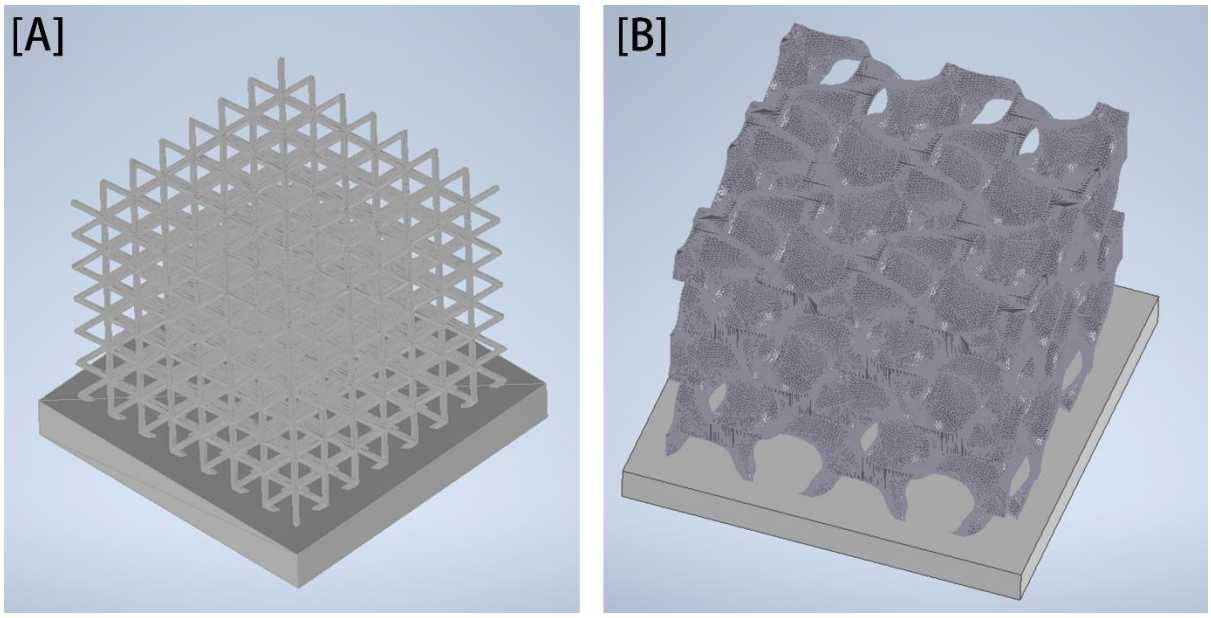

Figure S12. (A) The original cubic vertex centroid lattice structure ("lattice structure") and (B) the gyroid structure model for 3D printing

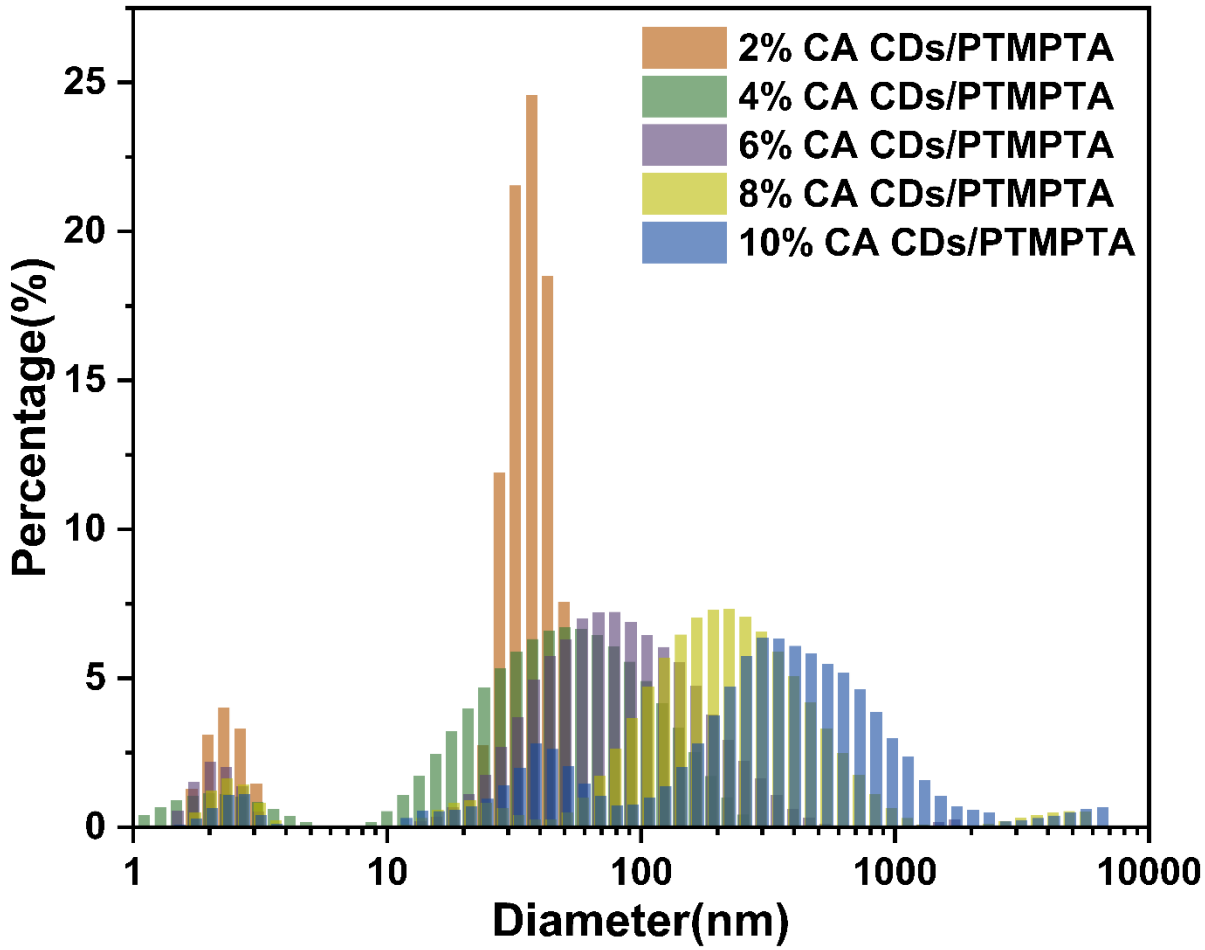

Figure S13. DLS test for particle size distribution of CA CDs in prepolymer solutions of all composites.

Table S2 Tensile Young's modulus of each sample of composites and PTMPTA

	Tensile modulus for PTMPTA (MPa)	*Tensile modulus for 2% CA CDs/PTMPTA composites (MPa)*	*Tensile modulus for 4% CA CDs/PTMPTA composites (MPa)*	*Tensile modulus for 6% CA CDs/PTMPTA composites (MPa)*	*Tensile modulus for 8% CA CDs/PTMPTA composites (MPa)*	*Tensile modulus for 10% CA CDs/PTMPTA composites (MPa)*
1	**190.735**	**306.463**	**402.373**	**416.805**	**375.452**	**351.227**
2	**294.536**	**304.931**	**360.272**	**408.506**	**364.449**	**435.849**
3	**225.065**	**307.505**	**360.207**	**430.572**	**369.063**	**437.048**
4	**244.281**	**255.516**	**340.259**	**426.368**	**336.321**	**373.452**
5	**276.05**	**280.949**	**329.314**	**390.17**	**352.765**	**380.723**
6	**234.709**	**309.963**	**363.12**	**386.996**	**375.452**	**350.761**
7	**225.05**	**285.888**	**415.844**	**355.61**	**369.063**	**430.83**
8	**232.176**	**260.207**	**365.584**	**381.189**	**358.862**	**415.499**
9	**240.777**	**294.48**	**357.282**	**444.767**	**371.426**	**341.218**
10	**244.393**	**302.835**	**309.885**	**371.22**	**364.17**	**384.15**
average	**240.7772**	**290.8737**	**360.414**	**401.2203**	**363.7023**	**390.0757**

Table S3 Compression Young's modulus of each sample of composites and PTMPTA

	Compression modulus for PTMPTA (Pa)	*Compression modulus for 2% CA CDs/PTMPTA composites (Pa)*	*Compression modulus for 4% CA CDs/PTMPTA composites (Pa)*	*Compression modulus for 6% CA CDs/PTMPTA composites (Pa)*	*Compression modulus for 8% CA CDs/PTMPTA composites (Pa)*	*Compression modulus for 10% CA CDs/PTMPTA composites (Pa)*
1	2.68767×10^{8}	4.24328×10^{8}	5.79987×10^{8}	6.79615×10^{8}	1.01637×10^{9}	4.94607×10^{8}
2	2.94933×10^{8}	4.34545×10^{8}	5.91994×10^{8}	7.70838×10^{8}	9.99498×10^{8}	1.04613×10^{8}
3	1.83065×10^{8}	4.16019×10^{8}	6.22531×10^{8}	7.4173×10^{8}	9.02662×10^{8}	1.79859×10^{8}
4	2.92963×10^{8}	4.24437×10^{8}	5.51577×10^{8}	7.88737×10^{8}	8.05973×10^{8}	1.84769×10^{8}
5	2.56002×10^{8}	4.46104×10^{8}	5.52181×10^{8}	7.11541×10^{8}	8.18884×10^{8}	1.13212×10^{8}
average	2.59146×10^{8}	4.29087×10^{8}	5.79654×10^{8}	7.38492×10^{8}	9.08678×10^{8}	2.15412×10^{8}

Table S4 Compression load-bearing capacity of each sample of composites and PTMPTA

	Compression max force for PTMPTA (N)	*Compression max force for 2% CA CDs/PTMPTA composites (N)*	*Compression max force for 4% CA CDs/PTMPTA composites (N)*	*Compression max force for 6% CA CDs/PTMPTA composites (N)*	*Compression max force for 8% CA CDs/PTMPTA composites (N)*	*Compression max force for 10% CA CDs/PTMPTA composites (N)*
1	5490	8058	10050	15599	19412	3998

2	5411	8132.9	12115	14430	17768	3358.3
3	4508.8	6990.8	12195	14785	17860	3135
4	5513.9	7098.48	9913.84	15459	20703	3835
5	6019.7	8393.3	12444.8	14737	17747.9	2263
average	5388.68	7734.696	11343.728	15002	18698.18	3317.86

Table S5 The print resolution of composites and PTMPTA

TARGET (*l* × *w*=480 *μm* × *100 μm)*	***l* (μm)**	***w* (μm)**
PTMPTA	**-**	**-**
2% CA CDS/PTMPTA COMPOSITES	**-**	**-**
4% CA CDS/PTMPTA COMPOSITES	258.2 ± 59.1	571.2 ± 74.5
6% CA CDS/PTMPTA COMPOSITES	426.8 ± 11.8	163.7 ± 15.5
8% CA CDS/PTMPTA COMPOSITES	476.3 ± 14.3	117.4 ± 13.3
10% CA CDS/PTMPTA COMPOSITES	**-**	**-**

- : Unable to replicate the designed structure.

References

[1] P. Thangaraju and S. B. Varthya, 'ISO 10993: Biological Evaluation of Medical Devices', in *Medical Device Guidelines and Regulations Handbook*, P. S. Timiri Shanmugam, P. Thangaraju, N. Palani, and T. Sampath, Eds., Cham: Springer International Publishing, 2022, pp. 163–187. doi: 10.1007/978-3-030-91855-2_11.

[2] Y. Dong *et al.*, 'Blue luminescent graphene quantum dots and graphene oxide prepared by tuning the carbonization degree of citric acid', *Carbon*, vol. 50, no. 12, pp. 4738–4743, Oct. 2012, doi: 10.1016/j.carbon.2012.06.002.

[3] X. Miao *et al.*, 'Synthesis of Carbon Dots with Multiple Color Emission by Controlled Graphitization and Surface Functionalization', *Adv. Mater.*, vol. 30, no. 1, p. 1704740, 2018, doi: 10.1002/adma.201704740.

[4] J. Guo *et al.*, 'Yellow-Emissive Carbon Dots with High Solid-State Photoluminescence', *Adv. Funct. Mater.*, vol. 32, no. 20, p. 2110393, 2022, doi: 10.1002/adfm.202110393.

[5] 'NMR Chemical Shift Values Table - Chemistry Steps'. Accessed: Dec. 02, 2024. [Online]. Available: https://www.chemistrysteps.com/nmr-chemical-shift-values-table/

[6] '13C Carbon NMR Spectroscopy - Chemistry Steps'. Accessed: Dec. 02, 2024. [Online]. Available: https://www.chemistrysteps.com/13c-carbon-nmr-spectroscopy/

[7] K. Chang, Q. Zhu, L. Qi, M. Guo, W. Gao, and Q. Gao, 'Synthesis and Properties of Nitrogen-Doped Carbon Quantum Dots Using Lactic Acid as Carbon Source', *Materials*, vol. 15, no. 2, p. 466, Jan. 2022, doi: 10.3390/ma15020466.

[8] A. Theodosiou, B. F. Spencer, J. Counsell, and A. N. Jones, 'An XPS/UPS study of the surface/near-surface bonding in nuclear grade graphites: A comparison of monatomic and cluster depth-profiling techniques', *Appl. Surf. Sci.*, vol. 508, p. 144764, Apr. 2020, doi: 10.1016/j.apsusc.2019.144764.

[9] Y. Liu, D. Chao, L. Zhou, Y. Li, R. Deng, and H. Zhang, 'Yellow emissive carbon dots with quantum yield up to 68.6% from manganese ions', *Carbon*, vol. 135, pp. 253–259, Aug. 2018, doi: 10.1016/j.carbon.2018.02.004.

[10] M. A. Sk, A. Ananthanarayanan, L. Huang, K. H. Lim, and P. Chen, 'Revealing the tunable photoluminescence properties of graphene quantum dots', *J. Mater. Chem. C*, vol. 2, no. 34, pp. 6954–6960, Aug. 2014, doi:

10.1039/C4TC01191K.
[11] S. Zhu, Y. Song, X. Zhao, J. Shao, J. Zhang, and B. Yang, 'The photoluminescence mechanism in carbon dots (graphene quantum dots, carbon nanodots, and polymer dots): current state and future perspective', *Nano Res.*, vol. 8, no. 2, pp. 355–381, Feb. 2015, doi: 10.1007/s12274-014-0644-3.
[12] F. Oustadi, R. Imani, M. Haghbin Nazarpak, and A. M. Sharifi, 'Genipin-crosslinked gelatin hydrogel incorporated with PLLA-nanocylinders as a bone scaffold: Synthesis, characterization, and mechanical properties evaluation', *Polym. Adv. Technol.*, vol. 31, no. 8, pp. 1783–1792, 2020, doi: 10.1002/pat.4905.
[13] G. Hoti *et al.*, 'Effect of the Cross-Linking Density on the Swelling and Rheological Behavior of Ester-Bridged β-Cyclodextrin Nanosponges', *Materials*, vol. 14, no. 3, p. 478, Jan. 2021, doi: 10.3390/ma14030478.
[14] S. L. Tomić *et al.*, 'Manuka Honey/2-Hydroxyethyl Methacrylate/Gelatin Hybrid Hydrogel Scaffolds for Potential Tissue Regeneration', *Polymers*, vol. 15, no. 3, Art. no. 3, Jan. 2023, doi: 10.3390/polym15030589.
[15] R. Wang, C. Cheng, H. Wang, and D. Wang, 'Swollen hydrogel nanotechnology: Advanced applications of the rudimentary swelling properties of hydrogels', *ChemPhysMater*, vol. 3, no. 4, pp. 357–375, Oct. 2024, doi: 10.1016/j.chphma.2024.07.006.